American Journal of Astronomy and Astrophysics
2024, Vol. 11, No. 3, pp. 65-73
https://doi.org/10.11648/j.ajaa.20241103.11

Research Article

Assessment of Background Radiation Levels on the Lunar Surface and Mapping the Lunar Albedos

Subhojit Halder*, Aarya Kulkarni, Atharva Thakur

Department of Electronics and Telecommunication Engineering, College of Engineering Pune (COEP), Pune, India

Abstract

This literature explores the impact of Galactic Cosmic Radiation (GCR) and Solar Energy Particles (SEP) on lunar surface radiation levels, using data from OLTARIS and CRATER missions. Applying the Focker-Planck equation with Badhwar-O-Neil 2020 constraints, we predict radiation levels for 53 ionic particles. The Ap-8 min model addresses trapped protons and neutron albedo on the lunar regolith. ACE/CRIS's spectrometer data determines the Isotopic Composition of GCR, generating Linear Energy Transfer (LET) plots. CRATER and OLTARIS data characterize high-energy particles above the lunar surface. A spherical harmonic Lambertian surface is generated, on which contours representing scaled reflectance are obtained by passing the data through a Gaussian kernel. ARIMA and Random Forest machine learning models predict parameters, and HZETRN2020 and OLTARIS data produce an albedo map of the lunar regolith. This research aims to enhance radiation protection strategies for future lunar missions and space exploration. The value of scaled reflectance and radiation plots have been generated to help understand the impact of the predominant 53 ionic particles covering the range from solar activity particles SEP to the galactic radiation GCR. The values are provided by running various stimulations under multiple constraints provided in OLTARIS, and the value of these stimulated results are mapped across the lunar surface ranging from -180 degrees to 180degree by -90degree to 90degree plot, giving an accuracy up to 1895.21 px/m with a resolution of 16 degree per pixel in the generated radiation plot. The radiation flux developed provides a concise and detailed understanding of the nature of radiation entrapment on the lunar regolith. It successfully translates the lunar albedo value as per the scaled reflectance on the surface.

Keywords

Lambertian Surface, Scaled Reflectance, Lunar Albedo, SEP, GCR

1. Introduction

Exploration and potential habitation of the Moon have become increasingly important goals in the realm of space exploration. One of the critical challenges associated with lunar missions is the effect of radiation on the lunar surface. Understanding the radiation levels on the Moon is essential for ensuring the safety and well-being of astronauts and equipment during extended stays or permanent settlements [1]. This paper studies the effect of GCR (Galactic Cosmic Rays) and SEP (Solar Energy Particles) on the lunar surface. Data from OLTARIS and Cosmic Ray Telescope Effects for Radiation (CRATER) missions is used. The Badhwar-O-Neil, 2020 constraints [2] operate on the obtained data. The BON2020 model facilitates analysis by taking into account 53 ionic particles including protons, electrons, alpha particles

*Corresponding author: subhojith90@gmail.com (Subhojit Halder)

Received: 12 August 2024; **Accepted:** 2 September 2024; **Published:** 23 September 2024

and heavier ions of carbon, oxygen and nitrogen. Employing the Focker-Planc equation [3], integral and differential flux of ionic particles are generated. The flux interpolations help determine dose rates and their equivalents on lunar surface. For analyzing the trapped proton and neutron model in a surface the manuscript uses a method named as AP- model. The Ap-8 model provides a comprehensive understanding of the omnidirectional trapped proton and neutron concentration in a lower orbit of the magnetosphere but by changing the parameters in the model it can be applied to find the trapped proton and neutron particles for a celestial object. There are 2 formats by which this model can be applied, Ap-8 min model and Ap-8 max model, the manuscript uses the AP-8min mode as it helps in shedding a better understanding of the trapped protons in the solar minimum conditions. The Ap-8 min model considers trapped protons and neutron albedo on the lunar regolith. By eliminating errors and redundancies, this model streamlines the assessment of radiation levels on the lunar surface. The isotopic composition of GCR data, obtained from the ACE/CRIS spectrometer [4], facilitates the generation of Linear Energy Transfer (LET) integral and differential flux plots., enhancing the understanding of the lunar radiation environment. Data taken from the Chang'E4 lander processed with Beer-Lambert's law provides insight into the relation between the penetration depth of radiation on lunar surface and radiation intensity [5]. In addition to GCR and SEP, the research explores parameters characterizing high-energy particles above the lunar surface, such as magnetic field, orientation, density, speeds, and temperature. CRATER and OLTARIS data are processed to provide valuable insights into these parameters. To predict the nature of these parameters, the study primarily employs ARIMA and Random Forest machine learning prediction models. These models process training data and operate on test data, to model the behavior pattern of the parameters with respect to time and predict future behavior [6, 13]. The Lambertian surface of the moon is obtained which depicts iso-brightness contours on the lunar regolith. Data interpolated from HZETRN2020 and OLTARIS provides values of scaled reflectance on the lunar surface and is mapped onto the Lambertian surface of the moon [7]. Contours in the scaled reflectance plot are obtained by subjecting the calibrated Lambertian surface $L(\theta, \emptyset)$ to Gaussian kernel smoothing. This process enhances signal-to-noise ratio, facilitating contour identification critical for analyzing geographic variations in the reflectance map [22]. The lunar albedo generated provides valuable insights into the lunar radiation environment.

2. Methodology and Analysis

Spectroscopic observations on the lunar surface, as exemplified by the Chang'E-3 (CE-3) missions in situ reflectance spectra obtained by the Visible-Near Infrared Spectrometer (VNIS), play a pivotal role in unravelling key lunar properties [7].

The dynamic nature of the lunar environment as identified by the substantial differences in reflectance spectra between the uppermost soil layer and the material immediately beneath underscores the complexity of lunar surface composition. Traditional methods of lunar sample analysis thus fall short of accuracy of the simulation of a lunar surface.

It is imperative that accurate predictions of lunar surface irradiance of solar energy particles are necessary for detailed study. An albedo provides detailed insights in this regard. Albedo refers to the measure of a surface's reflectivity, indicating the proportion of incoming light that is reflected by the surface [11]. It is a bi-hemispherical property, accounting for the reflection of solar radiation from both the illuminated and shadowed parts of the surface. Albedo values range from 0 (complete absorption, no reflection) to 1 (total reflection) [12]. From a radiation equilibrium perspective, the lunar atmosphere has minimal impact on surface albedo. When exposed to pure diffuse radiation, the reflectivity of a surface conforms essentially to Lambertian behavior [8]. When objects are Lambertian, a simple, three-to-seven-dimensional linear subspace can capture the set of images they produce [9, 13]. The set of lunar images obtained were approximated to 91.3 percent by a 3D space and to 99.2 percent by a 7D space. Render the images of an object and find an 11D subspace that approximates these images. These numbers are roughly comparable to the 9D space that, according to our analysis, approximates the images of a Lambertian object [9, 14]. Considering multiple observation points for the generation of the scaled reflectance map of the lunar surface, 2 types of Lambertian surfaces were considered for the development of iso-brightness contours for localizing and segmenting the points and regions with higher reflectance. The other Lambertian surface generated is with the spherical harmonic approximation method which allows for multiple unknown light sources and attached shadows [15, 16].

Spherical coordinates

$$x = \sin(\theta)\cos(\emptyset)$$

$$y = \sin(\theta)\sin(\emptyset)$$

$$z = \cos(\theta)$$

The spherical harmonic function is represented with degree L, order M and P_L^M representing Legender Polynomial.

$$Y_L^M(\theta, \emptyset) = \sqrt{\frac{(2L+1)(L-M)!}{4\pi(L+M)!}} P_L^M \cos(\theta)\, e^{iM\emptyset}$$

Thus, the corresponding Lambertian Surface comes to be:

$$L = \sum_{L=0}^{\mu-1} \sum_{M=-L}^{L} \gamma[L, M] \times Y_L$$

where, μ coefficient value and $\gamma[L, M]$ is the spherical harmonic coefficient. Normalizing the data for Lambertian

surface,

$$\alpha(u,v) = normalize\left(u\left|\left|M\right|\right|, v\left|\left|N\right|\right|\right)$$

M and N are dimensions of Lambertian surface. Lambertian surface with environmental map provides

$$Y_I(\theta,\emptyset) = R_e\left(\sum_{L=0}^{L-1}\sum_{M=-L}^{L}\gamma[L,M] \times Y_L^M(\theta,\emptyset)\alpha(u,v)\right)$$

The evaluation of these parameters and proceeded with taking the general spherical coordinates and evaluating the spherical harmonic coefficients $\gamma[L,M]$ are computed using the formula for spherical harmonics for each coefficient with degree L and order M where P_L^M is the associated Legendre polynomial. Generate a normalized and resized environment map with the exact dimensions of the Lambertian surface. Combining the Lambertian surface with the resized environment map involves integrating the product of the Lambertian surface and the environment map over the sphere's surface. The summation represents the combination of multiple harmonics. In this case, the integral is implicit in the spherical harmonic representation, and the pixel-wise product integrates over the entire sphere. Figure 1 presents the results of the generated approximation for the Lambertian surface. This Lambertian reflectance functions as a straightforward low-pass filter on data, facilitating a nuanced understanding. Utilizing this simplicity, the constructed model for processing dynamic reflectance on the lunar surface. The data enables us to determine the Lambertian surface. The Lambertian surface provides the mapping of iso-brightness contours.

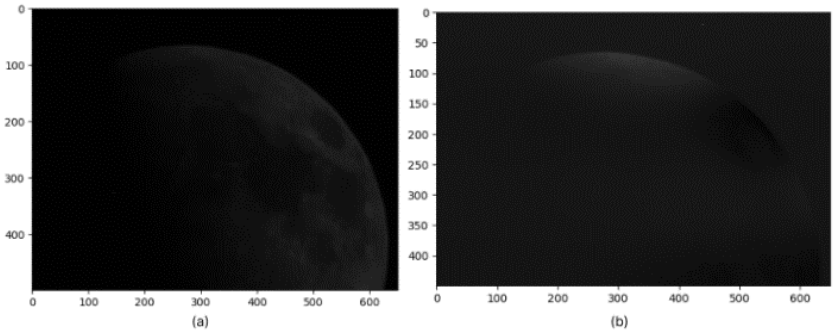

Figure 1. *Represents the Lambertian surface generated with passing through a Lambertian surface generated with a linear space with 3D and 7D coefficient approximation (a) and using the spherical harmonic model approximation (b).*

Iso-brightness contours refer to lines or curves on a graphical representation of an image or a map that connect points of equal brightness or intensity. These contours are used to visualize regions of an image or a scene where the brightness levels are consistent [17, 18]. In the context of remote sensing, iso-brightness contours are valuable for understanding and analyzing variations in reflectance across a landscape, helping to identify features with similar reflective properties [19]. They provide a visual representation of uniform brightness levels, aiding in the interpretation of images and the identification of patterns or structures based on their reflective characteristics. An image motion model exists for the computation of optical flow, which permits brightness variation of an image point from one instant of time to the next, in the form of a linear transformation involving multiplier and offset fields [10]. The iso-brightness contours obtained from the Lambertian surface thus provide a simplified medium to measure changes in reflectance on the lunar regolith. Contour regions are mapped on the surface for this purpose. These isolated points help in understanding the variation of the scaled reflectance and albedo of the region targeted [20]. Image calibration post Lambertian surface

$$L_{IC}(\theta,\emptyset) = \frac{L_1(\theta,\emptyset)}{T \times G}$$

where T= exposure time, G = Telescope gain. Applying Gaussian filter for smoothening data and finding contours,

$$G_\sigma(u,v) = \frac{1}{2\pi\sigma^2}e^{-\frac{u^2+v^2}{2\sigma^2}}$$

$$G_\sigma(u,v) = \frac{1}{2\pi\sigma^2}e^{-\frac{sin^2(\theta)}{2\sigma^2}}$$

$$S(\theta,\emptyset) = L_{IC}(\theta,\emptyset) * G_\sigma(\theta,\emptyset)$$

After passing the calibrated Lambertian image through the Gaussian filter, we land with the smoothened image represented by $S(\theta,\emptyset)$. The thresholds are generated using this by ranging it from the minimum to maximum value of the smoothened data by keeping a base threshold represented as T and the threshold array of the values is T_v. The obtained contours are represented by C_v.

$$T_v \in \left(Min\left(S(\theta,\emptyset)\right), Max\left(S(\theta,\emptyset)\right)\middle| T \to R\right)$$

$$C_v = (S(\theta,\emptyset)|S(\theta,\emptyset) \in T_v)$$

The Lambertian surface generated $L(\theta,\emptyset)$ from the FITS

file is calibrated by factors like exposure time T and telescope gain G to remove the redundancies that can be created and to generate a normalized data plot for creating a Lambertian Surface. Calibration involves adjusting the pixel values to represent physical radiance or reflectance values. The calibrated reflectance map generated is then smoothened by passing to the Gaussian kernel. Gaussian kernel smoothing is a simple and effective technique for reducing noise in the generated Lambertian surface to identify the distinct contours, increasing signal-to-noise ratio and smoothness for statistical inference [21]. For smoothening the data, the generated Lambertian surface is convolved with the gaussian kernel. The generated smoothened data is used to calculate the threshold values for the contours where T represents the threshold level to keep generated by the trained model. Figure 2 shows a detailed results of the generated contours from the plain Lambertian surface passing through the low pass filter with linear space of 3D and 7D subspaces which provides an isolation of brightness regions and would play a crucial role for generation of the scaled reflectance plot and using the gradient on these contour regions the corresponding geographic variations of the scaled reflectance can be observed.

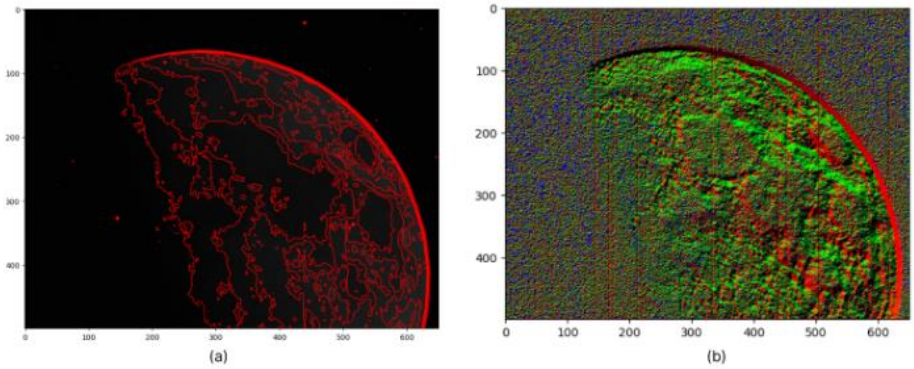

Figure 2. *Contours generation for isolating darkness pass on the generated spherical harmonic Lambertian surface (a) and the reflectance mapping of the generated brightness contours for isolating the heavy ionic reflectance (b).*

The data plots obtained from training the model with the differential LET model obtained from OLTARIS considering a 1002 ray traced thickness where a set of directionally emerging rays from the same point is considered to determine the thickness penetration through any ray in a particularly given direction [22, 23]. The gradient plot observed in the Figure 2(b) is obtained by training the contour models with Flux (particles/(AMeV-day-cm2)) vs. Energy (AMeV) with consideration of 9 radiative particles were considered at Target source of Lunar regolith, Figure 3 provides the energy to flux plot of these values and there effects in logarithmic x and y scale these values are used for training the model for the remaining plots the gradient descent with green tangent shows he region with flux interpolation taking Lunar Albedo Effects into considerations. The LET (Linear Energy Transfer) values obtained from the ACE/CRIS spectroscopic observatory helps in creating a finer graph slope that provides the clean particle interpolation of flux, the graph presented in Figure 3 provides the target source has a dose rate at 2.029E-01 mGy per day due to GCR effects from the free space and the net lunar albedo effect albedo 4.851E-02 mGy. The Fokker-Planck equation is a partial differential equation that describes the time evolution of a probability density function associated with the continuous random motion of particles or a stochastic process. The Fokker-Planck equation describes the time evolution of the probability distribution of a stochastic process on a Euclidean space [28, 29]. The calculated values are obtained by solving the derived of Foker-Planck equation also named as Badhwar−O'Neill 2020 (BON2020) GCR Model. $\emptyset(t)$ the solar modulation potential and considering the fixed values of the constants V_{SW}=400 km/s, $r_0 = 4\,AU$, and $k_0 = 8.81020 cm^2/s$ [2, 24].

$$\frac{k(r,t)}{V_{sw}} = \frac{\beta R k_0}{\emptyset(t) V_{sw}} \left[1 + \left(\frac{r}{r_0}\right)^2\right]$$

The model is trained with the Random Forests regression model which combines multiple individual decision tree regressors to create a more robust and accurate predictive model for calculating the reflectance variations as observed in the Figure 2(b) [25]. Setting up one variable as the target and the others as features of the target, the train data is now a function of the target as well as the features, feature selection is an important research direction in the field of statistical machine learning, which is central to improving model training speed and classification accuracy and to enhance the interpretability of model results. Too many or too few dimensions of the features, or features without enough importance will eventually to some extent, lead to the poor generalization of the training model [26]. We have used 3-4 parameters as features for our target variable as per the necessity for the model to fit onto the dataset, this trained data is now accessed by the Random Forest Regressor model for model fitting.

$$MSE = \frac{1}{T_v} \times \sum_{i \in m} \left(C_{v_i} - C_{v_m}\right)^2$$

The predicted value –

$$y = \frac{1}{T_v} \times \sum_{i=1}^{T_v} f_i(x)$$

where $f_i(x)$ is prediction of the I term. The predicted values obtained from this dataset is then used to form a basis for mapping the gradients of the iso-brightness contours obtained.

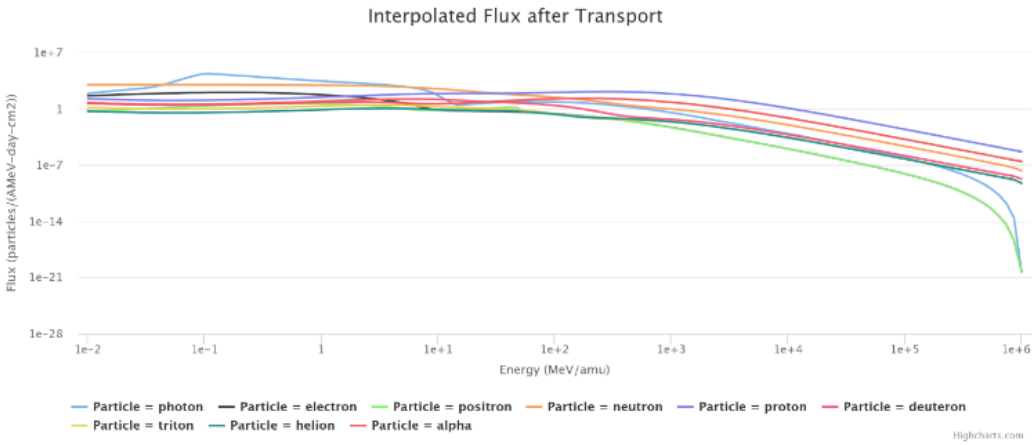

Figure 3. *Graphical representation of lux (particles/(AMeV-day-cm^2)) vs. Energy (AMeV) for 9 major particles captured for interpolation of calculation of the net effect of GCR on the Lunar regolith.*

For a complete and in-depth analysis of all the region and to calculate the reflectance properties of the lunar regolith to evaluate this spectroscopic analysis the NIR spectroscopic dataset provides a detailed analysis of the Spectroscopic measurements done for each specific regions of the lunar surface [27]. The dataset generated is based on the mission and from NASA archives of 1998. This model of data when aligned with the current flux interpolation provided by solving the derivation of the Focker-Planck equation for a 3D sub-space we observe a change in the randomness of the motion by applying constant volume measurements to figure out the randomness of the particles just before collision provides a unified solution into how the particles behave just before collision [31].

The 3D Focker Plank equation is given by –

$$\frac{\partial f(r,t)}{\partial t} = D\nabla^2 f(r,t)$$

where $D\nabla^2 f(r,t)$ deals with the random motion of particles in free space. Incorporating Flux and Energy values,

$$\frac{\partial f(r,t)}{\partial t} = D\nabla^2 f(r,t) - \nabla \cdot \left(\emptyset(r,t) f(r,t)\right) + \nabla \cdot \left(D\nabla E(r,t) f(r,t)\right)$$

Using Maxwellian distribution to understand the effects of movement of random particles –

$$f(v) = \left(\frac{m}{2\pi K_b T}\right)^{3/2} \times e^{-\frac{mv^2}{2K_b T}}$$

A product of 3 dimensional vectors and solving for the 3-dimensional equation with respect to position and time, the random motion and density of these particles at any given location in space is accounting for using $\eta(r,t)$.

$$f(r,v,t) = \eta(r,t)\left(\frac{m}{2\pi K_b T(r,t)}\right)^{3/2} \times e^{-\frac{m|v|^2}{2K_b T(r,t)}}$$

Considering variational mass for all available particles,

$$f(r,v,t) = \sqrt{\frac{8}{\pi^3}} \sum_i \eta_i(r,t)\left(\frac{m_i}{K_b T_i(r,t)}\right)^{3/2} \times e^{-\frac{m_i|v-u_i(r,t)|^2}{2K_b T_i(r,t)}}$$

where $\eta(r,t)$ is the corresponding particle density coefficient Taking for idealistic stationary consideration, motion independent equation turns out to be –

$$f(r,t) = \sqrt{\frac{8}{\pi^3}} \sum_i \eta_i(r,t)\left(\frac{m_i}{K_b T_i(r,t)}\right)^{3/2}$$

Solving with the initial boundary conditions at t=0, at boundary condition the flux and energy operators acts constant without any change and the velocity of those particles at that instance is bounded by u(r,0). The differential equation becomes –

$$\frac{\partial f(r,0)}{\partial t} = D\nabla^2 f(r,0) - \Phi(r,0)\nabla f(r,0) \mid_{t=0}$$

At the boundary condition, the equation turns out to be –

$$\frac{\partial f(r,0)}{\partial t} = 0 \mid_{t=0}$$

Using the Maxwellian distribution for consideration of the randomness of the motion in 3D subspace to figure out the solution of the probability density curve of the Focker-Planck equation gives a result into how many active particles are colliding into the lunar regolith in any given instant of time. The relativistic Maxwellian distribution provides a new probability distribution for astrophysics, with applications to random motion of multiple particles at controlled environment temperature of free space [30]. The derived Focker-Planck equation contains the solution for all the components corresponding to the flux and energy that provides a unified relation to understanding the absorbance of the particles in the lunar surface at a specific wavelength of spectrometer. The flux term accounts for the directed motion of particles, potentially towards or away from regions on lunar soil. The energy term introduces a bias in particle motion based on the local energy landscape. This takes in consideration of the interparticle attraction and the generation of the potential around the targeted surface region due to the emission of flux. The divergence of the product of the gradient of the energy field and the Maxwellian distribution function represents how the spatial distribution evolves based on the energy landscape. This term introduces a bias in particle motion based on the local energy. While the negative divergence of the product of the flux and the Maxwellian distribution function represents how particles move in response to the flux. This term introduces a directed motion in the direction of the flux. the scaled reflectance R represents the ratio of reflected radiant flux to the incident radiant flux [32]. The product of the value of scaled reflectance for a particular region with the corresponding flux and energy equations provides a detailed analysis of interaction of these particles with the surface of the lunar regolith [33]. Scaled reflectance –

$$\| R \| = \sum_i R_i$$

$\| R \|$ represents the average of specific scaled reflectance in the region –

$$L_{flux_{interaction}} = \| R \| \frac{\partial f(r,t)}{\partial t} |_{v=0}$$

The values obtained from [27] is incomplete at certain coordinate range and these missing values are obtained by training an ARIMA model with the training correlation data between the trained regions and the contours obtained in the figure 2. Correlating these datasets provides a generation of data for remaining coordinate system for mapping between these products as obtained in the equation 26. The Autocorrelation and the Partial Autocorrelation plots are used to determine the p, d, and q parameters of the ARIMA model [34]. Autocorrelation and Partial Autocorrelation Functions (ACF and PACF) are used to identify the correlation structure in time series data. They help us understand the relationships between the observations at different time lags and aid in determining the order of autoregressive (AR) and moving average (MA) components in ARIMA models. ACF plots show how correlated the time series is with its past values (lags). If the ACF plot shows a significant positive correlation at a specific lag and then decreases to zero as lags increase, it suggests that there is a potential MA term at that lag. In our case, the Autocorrelation plot is a discrete-valued function ranging from 1 and descending after each interval to a range between 0.5 and 0, which suggests that there may be a potential moving average term present, this further suggests that p may take values greater than 1. There is a slowly decaying correlation with the past lags and this lag remains constant for the future values of the data. This pattern is common in time series data with a mild trend or seasonal patterns. It suggests that past values can provide useful information for forecasting future values. An approach of using the AIC (Akaike Information Criterion), it is used for model selection and comparison in the context of time series analysis, such as in the case of ARIMA models. AIC is calculated based on the likelihood function of the model and the number of parameters used in the model [35].

The goal when using AIC is to find the model that minimizes this criterion, as a lower AIC score indicates a better trade-off between fitting the data well and using fewer parameters. In practical terms, we can compare different ARIMA models by calculating their respective AIC scores and selecting the model with the lowest AIC value. A limit is set on the value of each parameter since higher values of the parameters are avoided, as they result in higher error percentage data, in our case the values are restricted between 1 to 3, since by trial and error, a trivial solution is not obtained as a value for the parameter, and 0 is neglected. Upon comparison with the range 1 to 3 and 1 to 4, both result in the same solution set for the parameters, i.e. (2,1,3). Hence total of 27 possible outcomes are expected, out of which 7 are selected based on the least AIC score both result in the same solution set for the parameters, i.e. (2,1,3) the remaining values of AIC are shown in Table 1 [36].

Table 1. *The obtained AIC confidence values for the prefered paramets obtained from AIC model.*

Preferred values of the Parameters (p,d,q) respectively as calculated by the AIC Measure	Values of AIC coefficient
(1,1,1)	2350.7399152258577
(1,1,2)	2352.35965548928
(1,1,3)	2350.889162358925
(2,1,1)	2348.1759425833716
(2,1,2)	2350.1489578203823
(2,1,3)	2345.1653818888644
(2,2,2)	2358.4807406913496

Applying the AIC measure to the model, we obtain the best AIC value as 2345.1653818888644 and the best parameters as (2, 1, 3) for (p, d, q) respectively. The dataset is fit onto the model to predict future values. The obtained order is 6 for the parameter values (the value of the product pdq is defined as the order of the ARIMA model) hence it is an order 6 ARIMA model with a moving average value of 2, the future values are predicted, but adjusting the future value to a length that covers the entire dataset, so that the majority of the data is fit onto the model for better results. Two loops iterate over each combination of (p, d, q) one for calculating the most suitable and least value for the parameters as per the best AIC value and the other for fitting the model onto the parameters as obtained from the earlier loop. Within the loop, if the model fitting is successful and the calculated AIC value is smaller than the current AIC, the best AIC and best value for parameters are updated with the new values. The loop is made to continue in case of any error and ends only after obtaining the best AIC and the best parameter value [37]. Using inbuilt modules in Python for ARIMA modelling on a dataset, the Autocorrelation and Partial Autocorrelation plots are found. With the help of these plots along with the idea of AIC (Akaike Information Criterion) which is a statistical measure that compares different models based on the p, d, and q parameters. It returns the most appropriate values for the parameters; by measuring the AIC quotient, the algorithm compares the least AIC quotient and returns the p, d, and q parameters to fit onto the model. As per the results, the values of p, d, and q parameters as 2, 1, and 3. The model is then fit onto the data frame with the value of the above parameters. The plot of the Actual values versus the Predicted values are obtained and the Mean squared error is calculated to be 1.72 and the percentage error for this model is 18.53%. Parsing these predicted values into the system of equations derived from the Focker-Plank equation gives a set of values for each coordinate spectrum and the same information is been superimposed on a cylindrical image of moon taken by the Lunar Reconnaissance Orbiter Camera as shown in Figure 4 provides the final plot of the equation and shows an image with detailed understanding of interaction of Flux with the surface of the Lunar Regolith. The spots closer to brighter region resembling with white spots provides an insight of higher reflectivity of that region of the lunar surface whereas the darker spots closed to black shows a region with more absorbance of radiation as the scaled reflectivity values are less showing higher absorbance and less reflectance. The figure 4 is obtained by mapping the values obtained from the ARIMA trained model for corresponding latitude and longitude coordinates on a cylindrical image of the surface of the moon.

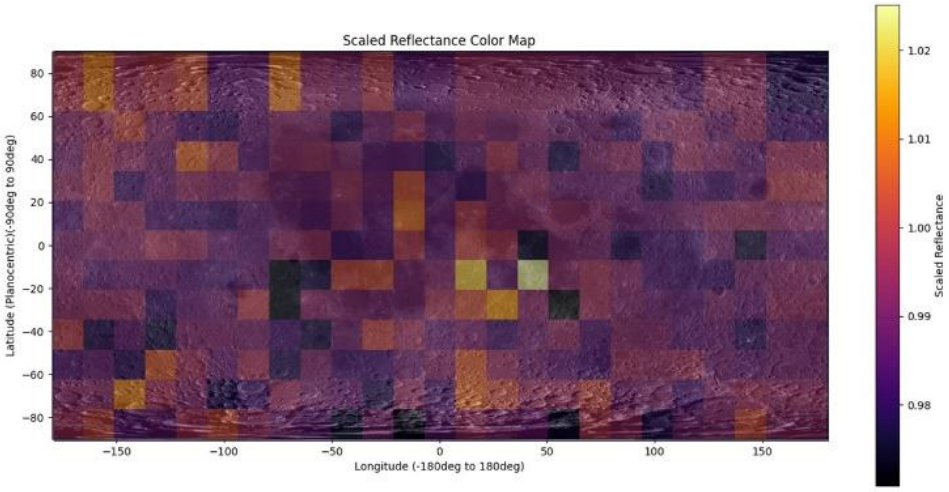

Figure 4. *Radiation flux plot for lunar regolith mapped on a Lunar cylindrical image with latitudes ranging from -90 to 90 and longitudes from -180 to 180 at co-ordinate with a resolution of 16.00 px/deg scaled at 1895.21 m/px.*

The corresponding change in surface flux interaction is mapped in the form of an inferno map. The understanding of the scaled reflectance can be understood from Figure 4 and it indicates the regions of the moon with the corresponding thermal characteristics of the region and the impact of radiation. The more the scaled reflectance the higher the ratio of particles hitting the surface to getting absorbed proving a higher radiation and dose rates in the regions whereas the darker spots provide an understanding of higher absorbance with a smaller number of particles being reflected back to space and more density of particles being absorbed in the surface. The values of reflectance obtained from the contour regions are compared with the values of scaled reflectance. To validate, the results are cross-verified with the existing albedo map which depicts the proton to neutron ratio from the cosmic ray telescope for the effects of radiation as shown by Wilson et. al [38]. The acquired data not only disclose thermal characteristics, compositional details, and the impact of space weathering but also shed light on the calibration of optical instruments operating remotely. The revelation that the lunar

regolith's thermal properties deviate from theoretical models underscores the significance of on-site measurements in refining our understanding of the Moon's surface conditions. Moreover, the observed changes in brightness, attributed to the removal of fine particles by the lander's exhaust, highlight the dynamic nature of the lunar environment, challenging preconceived notions.

3. Conclusions

Analysis of interplay of Galactic Cosmic Radiation (GCR) and Solar Energy Particles (SEP) on lunar surface has provided LET flux plots. The study successfully predicts radiation levels and dose rates for different ionic particles impacting the lunar surface using ARIMA and Random Forest machine learning prediction models. The integration of diverse data sources has led to predictability of radiation environment on the lunar regolith. Comparing prediction model results with actual observations using past mission data from CRATER and OLTARIS enhances prediction reliability.

The study of scaled reflectance has generated an albedo map of the lunar surface which is a significant achievement, offering insights into safer areas for human habitation and scientific activities. The albedo provides a visual understanding of radiation across the lunar surface with real time data. The research contributes to the broader understanding of space environments and radiation effects, applicable to spacecraft design, astronaut safety protocols, and protective shielding technologies.

Abbreviations

SEP	Solar Energy Particle
GCR	Galactic Cosmic Radiation
BON20	Bhadwar O Niel Model 2020
LET	Linear Energy Transfer
AIC	Akaike Information Criterion

Author Contributions

Subhojit Halder: Conceptualization, Methodology, Formula Analysis, Project administration

Aarya Kulkarni: Data curation, Investigation, Visualization, writing;

Atharva Thakur: Software, Validation Data

Data Availability Statement

The data is available from the corresponding author upon reasonable request.

Conflicts of Interest

The authors declare no conflicts of interest.

References

[1] "Radiation Environment on the Moon: Prospects and Challenges for Human Missions" Authors: Wimmer-Schweingruber, R. F., K ̈ohler, J., and Zeitlin, C. Journal: Space Science Reviews Publication Year: 2016.

[2] Slaba, T. C. and Whitman, K. (2020a) 'The Badhwar-o'Neill 2020 GCR model', Space Weather, 18(6), pp. 1–28. https://doi.org/10.1029/2020sw002456.

[3] J. N. Elgin (1984) The Fokker-Planck Equation: Methods of Solution and Applications, Optica Acta: International Journal of Optics, 31:11, 1206-1207, https://doi.org/10.1080/713821438

[4] Calvin, T. and Saganti, P. (2007) 'Radiation Particle Flux Assessment: Ace/Cris Data', AIAA SPACE 2007 Conference amp; Exposition [Preprint]. https://doi.org/10.2514/6.2007-6052

[5] Luo, P. et al. (2022) 'First measurements of low-energy cosmic rays on the surface of the Lunar Farside from chang'e-4 mission', Science Advances, 8(2), pp. 1–6. https://doi.org/10.1126/sciadv.abk1760

[6] Ershov, E., Yudina, O., Vinogradova, L., & Shakhanov, N. (2020). EQUIPMENT CONDITION MODELING BASED ON RANDOM FOREST AND ARIMA MACHINE LEARNING ALGORITHM STACKING. *Cherepovets State University Bulletin*, 4, 32-40. https://doi.org/10.23859/1994-0637-2020-4-97-3

[7] Wu, Y., & Hapke, B. (2018, February). Spectroscopic observations of the Moon at the lunar surface. Earth and Planetary Science Letters, 484, 145–153. https://doi.org/10.1016/j.epsl.2017.12.003

[8] Gueymard, C. A., Lara-Fanego, V., Sengupta, M., & Xie, Y. (2019, April). Surface albedo and reflectance: Review of definitions, angular and spectral effects, and intercomparison of major data sources in support of advanced solar irradiance modeling over the Americas. Solar Energy, 182, 194–212 https://doi.org/10.1016/j.solener.2019.02.040

[9] Basri, R. and Jacobs, D. W. (2003) 'Lambertian reflectance and linear subspaces', IEEE Transactions on Pattern Analysis and Machine Intelligence, 25(2), pp. 218–233. https://doi.org/10.1109/tpami.2003.1177153

[10] Shahriar Negahdaripour, Chih-Ho Yu 'A Generalized Brightness Change Model for Computing Optical Flow', https://doi.org/10.1109/iccv.1993.378241

[11] Henderson-sellers, A., & Hughes, N. (1982). Albedo and its importance in climate theory. Progress in Physical Geography, 6, 1-44. https://doi.org/10.1177/030913338200600101

[12] Grenfell, T., & Maykut, G. (1977). The Optical Properties of Ice and Snow in the Arctic Basin. Journal of Glaciology, 18, 445 - 463. https://doi.org/10.3189/S0022143000021122

[13] Nguyen, H., Liu, S., & Do, M. (2013). Subspace methods for computational relighting. 8657. https://doi.org/10.1117/12.2011522

[14] A. Georghiades, P. Belhumeur, and D. Kriegman, “From Few to Many: Generative Models for Recognition Under Variable Pose and Illumination,” Proc. Int’l Conf. Automatic Face and Gesture Recognition, 2000.

[15] I. Kemelmacher-Shlizerman and R. Basri, "3D Face Reconstruction from a Single Image Using a Single Reference Face Shape," in IEEE Transactions on Pattern Analysis and Machine Intelligence, vol. 33, no. 2, pp. 394-405, Feb. 2011, https://doi.org/10.1109/TPAMI.2010.63

[16] R. Ramamoorthi and P. Hanrahan, “On the Relationship Between Radiance and Irradiance: Determining the Illumination from Images of a Convex Lambertian Object,” J. Optical Soc., vol. 18, no. 10, pp. 2448-2459, 2001.

[17] Sinclair, D. (2000). Smooth region structure: folds, domes, bowls, ridges, valleys and slopes. Proceedings IEEE Conference on Computer Vision and Pattern Recognition. CVPR 2000 (Cat. No. PR00662), 1, 389-394 vol. 1. https://doi.org/10.1109/CVPR.2000.855845

[18] Hagen, H., Schreiber, T., & Gschwind, E. (1990). Methods for surface interrogation. Proceedings of the First IEEE Conference on Visualization: Visualization `90, 187-193. https://doi.org/10.1109/VISUAL.1990.146381

[19] Holden, H., & LeDrew, E. (1999). Hyperspectral identification of coral reef features. International Journal of Remote Sensing, 20, 2545-2563. https://doi.org/10.1080/014311699211921

[20] Li, Y., Sun, X., Wang, H., Sun, H., & Li, X. (2012). Automatic Target Detection in High-Resolution Remote Sensing Images Using a Contour-Based Spatial Model. IEEE Geoscience and Remote Sensing Letters, 9, 886-890. https://doi.org/10.1109/LGRS.2012.2183337

[21] Chung, M. (2020). Gaussian kernel smoothing. ArXiv, abs/2007.09539.

[22] Mukherjee, T., Halder, S., & Sharma, S. Accurate, Comprehensive and Predictive Research on Emissions from an Active Region of Sun and the Effect of the Radiation Topology on the Lower Earth Orbit and the Damage to Human Tissues. (2023). In International Journal of convergence in healthcare (Vol. 3, Issue 2). Pratyaksha Medical Care LLP. https://doi.org/10.55487/9q149026

[23] Robert C. Singleterry Jr.; Steve R. Blattnig; Martha S. Clowdsley; Garry D. Qualls; Chris A. Sandridge; Lisa C. Simonsen; Tony C. Slaba; Steven A. Walker; Francis F. Badavi; Jan L. Spangler; Aric R. Aumann; E. Neal Zapp; Robert D. Rutledge; Kerry T. Lee; Ryan B. Norman; John W. Norbury (2011). OLTARIS: On-line tool for the assessment of radiation in space. 68(7-8), 1086–1097.

[24] Gautam D. Badhwar (1997). Supplement: Space Radiation Damage and Biodosimetry || The Radiation Environment in Low-Earth Orbit. Radiation Research, 148(5), S3–S10.

[25] Breiman, L. (2001). Random Forests. Machine Learning, 45, 5-32. https://doi.org/10.1023/A:1010933404324

[26] Machine Learning Fusion Multi-Source Data Features for Classification Prediction of Lunar Surface Geological Units - W Zuo, X Zeng, X Gao, Z Zhang, D Liu, C Li - Remote Sensing, 2022.

[27] Pieters, C., 120-COLOR LUNAR NIR SPECTROPHOTOMETRY DATA V1.0, MK88-L-120CVF-3-RDR-120COLOR-V1.0, NASA Planetary Data System, 1998 https://doi.org/10.17189/1519537

[28] Annunziato, M., & Borz ̨ A. (2018). A Fokker–Planck control framework for stochastic systems. EMS Surveys in Mathematical Sciences. https://doi.org/10.4171/EMSS/27

[29] Chow, S., Huang, W., Li, Y., & Zhou, H. (2011). Fokker–Planck Equations for a Free Energy Functional or Markov Process on a Graph. Archive for Rational Mechanics and Analysis, 203, 969. https://doi.org/10.1007/s00205-011-0471-6

[30] Zaninetti, L. (2020). New Probability Distributions in Astrophysics: IV. The Relativistic Maxwell-Boltzmann Distribution. International Journal of Astronomy and Astrophysics. https://doi.org/10.4236/ijaa.2020.104016

[31] Dubinova, A., & Trigger, S. (2011). Advances in the studies of anomalous diffusion in velocity space. arXiv: Statistical Mechanics.

[32] Xue, X., Jin, S., An, F., Zhang, H., Fan, J., Eichhorn, M., Jin, C., Chen, B., Jiang, L., & Yun, T. (2022). Shortwave Radiation Calculation for Forest Plots Using Airborne LiDAR Data and Computer Graphics. Plant Phenomics, 2022. https://doi.org/10.34133/2022/9856739

[33] Hodges, R. (2011). Resolution of the lunar hydrogen enigma. Geophysical Research Letters, 38. https://doi.org/10.1029/2011GL046688

[34] Garg, N., Soni, K., Saxena, T., & Maji, S. (2015). Applications of AutoRegressive Integrated Moving Average (ARIMA) approach in time-series prediction of traffic noise pollution. Noise Control Engineering Journal, 63, 182-194. https://doi.org/10.3397/1/376317

[35] N. Darapaneni, D. Reddy, A. R. Paduri, P. Acharya and H. S. Nithin, "Forecasting of COVID-19 in India Using ARIMA Model," 2020 11th IEEE Annual Ubiquitous Computing, Electronics & Mobile Communication Conference (UEMCON), New York, NY, USA, 2020, pp. 0894-0899, https://doi.org/10.1109/UEMCON51285.2020.9298045

[36] Mondal, Prapanna & Shit, Labani & Goswami, Saptarsi. (2014). Study of Effectiveness of Time Series Modeling (Arima) in Forecasting Stock Prices. International Journal of Computer Science, Engineering and Applications. 4. 13-29. https://doi.org/10.5121/ijcsea.2014.4202

[37] Zhang, S., Dai, L., Gao, Y., & Xia, Y. (2020). Adaptive interpolating control for constrained systems with parametric uncertainty and disturbances. International Journal of Robust and Nonlinear Control, 30, 6838-6852. https://doi.org/10.1002/rnc.5140

[38] Jody K. Wilson, Harlan E. Spence, Justin Kasper, Michael Golightly, J. Bern Blake, Joe E. Mazur, Lawrence W. Townsend, Anthony W. Case, Mark Dixon Looper, Cary Zeitlin, Nathan A. Schwadron, “The first cosmic ray albedo proton map of the Moon”, Journal of Geophysical Research, https://doi.org/10.1029/2011JE003921